The potential and challenges of thin-film electrolyte and nanostructured electrode for yttria-stabilized zirconia-base anode-supported solid oxide fuel cells

CrossMark

Ho-Sung Noh, Kyung Joong Yoon, Byung-Kook Kim, Hae-June Je, Hae-Weon Lee, Jong-Ho Lee, Ji-Won Son*

High-temperature Energy Materials Research Center, Korea Institute of Science and Technology, Hwarangno 14-gil 5, Seongbuk-gu, Seoul 136-791, Republic of Korea

HIGHLIGHTS

- The exact evaluation of YSZ-based anode-supported thin film-SOFCs is reported.
- A peak power density surpassing 500 mW cm^{-2} at 500 °C is achieved.
- Electrodes with enhanced properties are needed to further improve at low-T.

GRAPHICAL ABSTRACT
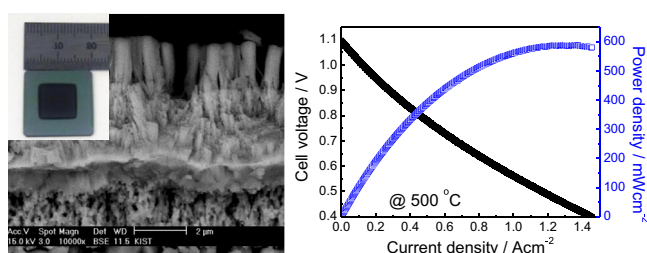
ABSTRACT

Thin-film electrolytes and nanostructured electrodes are essential components for lowering the operation temperature of solid oxide fuel cells (SOFCs); however, reliably implementing thin-film electrolytes and nano-structure electrodes over a realistic SOFC platform, such as a porous anode-support, has been extremely difficult. If these components can be created reliably and reproducibly on porous substrates as anode supports, a more precise assessment of their impact on realistic SOFCs would be possible. In this work, structurally sound thin-film and nano-structured SOFC components consisting of a nano-composite NiO–yttria-stabilized zirconia (YSZ) anode interlayer, a thin YSZ and gadolinia-doped ceria (GDC) bi-layer electrolyte, and a nano-structure lanthanum strontium cobaltite (LSC)-base cathode, are sequentially fabricated on a porous NiO–YSZ anode support using thin-film technology. Using an optimized cell testing setup makes possible a more exact investigation of the potential and challenges of thin-film electrolyte and nanostructured electrode-based anode-supported SOFCs. Peak power densities obtained at 500 °C surpass 500 mW cm^{-2}, which is an unprecedented low-temperature performance for the YSZ-based anode-supported SOFC. It is found that this critical, low-temperature performance for the anode-supported SOFC depends more on the electrode performance than the resistance of the thin-film electrolyte during lower temperature operation.

© 2013 Elsevier B.V. All rights reserved.

1. Introduction

Over the past decade, lowering the operation temperature of solid oxide fuel cells (SOFCs) has been intensively researched to avoid problems related to high temperature operations ($\geq$800 °C) such issues with the long-term stability, reliability, and cost [1]. In

* Corresponding author. Tel.: +82 2 958 5530; fax: +82 2 958 5529.
  E-mail addresses: jwson@kist.re.kr, jiwon.son@gmail.com (J.-W. Son).

addition, the low-temperature operation of SOFCs is a prerequisite for integrated and miniaturized SOFC systems (micro-SOFC) for high-performance portable and mobile power sources [2,3]. For these reasons, thin-film and nano-technologies, which are atypical of the field of SOFC, have been actively implemented to create the thin-film electrolyte and nanostructured electrode. This endeavor aims to lower the operation temperature of the SOFC without compromising performance by reducing the physical dimensions of the cell components without drastically changing the SOFC materials currently available.

The diverse research effort to form thin-film electrolyte and nanostructured electrode-based SOFCs (hereafter denoted as TF-SOFCs) can be classified into two major categories. One involves completely changing the SOFC cell platform to be compatible with thin-film technologies based on micro electro-mechanical system (MEMS) techniques. In this approach, an ultra-thin electrolyte and nano-porous electrode are fabricated on a platform formed via the back-side etching of rigid substrates, such as silicon wafers, which yields free-standing SOFC membranes less than a micron, or even a hundred nm, in thickness over an opening larger than 100 μm by 100 μm [3−12]. Remarkable and unprecedented low-temperature performance of such SOFCs, such as peak power densities of over 1 W cm^{-2} at 500 °C [3,5], have been reported using this platform. However, the mechanical frailty of such free-standing membranes, which are sensitive to the fabrication and operation conditions [13,14], and extremely poor long-term stability of the nano-porous noble metal electrodes [5,12,15] greatly restricts the cell component materials and fabrication methods available, resulting in highly variable performance for the cell [10]. In addition, obtaining a practical active area using a free-standing membrane design is extremely challenging, resulting in total power outputs of only micro-W despite the power density reaching over 1 W cm^{-2} [3]. Therefore, these technical hurdles must be overcome for free-standing SOFC platforms to be employed in practical working devices.

The other category of TF-SOFC uses TF-SOFCs over the currently available SOFC platforms, e.g., as anode supports, to achieve both high-performances at low-temperatures and thermo-mechanical stability. A thin-film electrolyte that forms over a porous support would possess better thermo-mechanical stability than one formed as a free-standing membrane. Such supports are expected to provide a larger cell area, more stable operations at elevated temperatures, and better resistance to thermal shocks; the mature stacking and system technologies of the present SOFC technologies can be directly utilized. Nevertheless, because it is difficult to create an ultra-thin electrolyte on a porous surface such as that of the anode support, obtaining gas-impermeable electrolytes with thickness equal to or less than 1 μm has been an elusive goal on this platform. Only recently have a few research groups reported success with this approach [16−21].

As one of the research groups that successfully synthesized a thin-film electrolyte over the anode support, the authors' group sequentially reported a successively improved cell performance for the anode-supported TF-SOFC since its initial realization [22]. On the basis of a newly developed nano-structure NiO−yttria-stabilized zirconia (NiO−YSZ) anode interlayer fabricated over sintered NiO−YSZ anode supports which are the common platform for conventional SOFCs, approximately 1 μm-thin electrolytes can be reliably fabricated [16,17,22]. The initial power density of 262.7 mW cm^{-2} at 0.7 V [22] was improved to 745.5 mW cm^{-2} at 600 °C by optimizing the microstructure of the supports and electrodes in a YSZ thin-film electrolyte-base cell [16]. Changing the electrolyte material to gadolinia-doped ceria (GDC) increased the power density to 988.9 mW cm^{-2} under the same conditions [17]. This result indicates the anode-supported TF-SOFC performance is affected by various factors, such as the electrode and support microstructures, electrolyte configurations, etc. Although substantial improvements in the performance have been achieved by optimizing the cell components, the ability to reach the critical performance at low temperature is hampered by external factors as well. One of these factors is loss from poor electrical contacts. Unlike free-standing membrane TF-SOFCs, where the performance is primarily measured by direct and close-contact to the very small cell area, anode-supported SOFC are tested for numerous issues that contribute to the contact resistance. It was reported that the total ohmic area specific resistance (ASR) was more than 5 times larger than the 1 μm-thick GDC/200 nm-thick YSZ bi-layer electrolyte resistance [17]. Because contact losses affect not only the ohmic ASR but also the polarization ASR (pol. ASR), a precise assessment of the effects of reducing the physical dimensions of the electrolyte and/or electrodes has been difficult.

To address this issue, a recent work by authors [23] varies the current collection configurations and materials to reduce the contact losses. When thin-film cathodes are used, the contact loss increases because the lateral conduction is disturbed by the crack-like pore shape. Therefore, optimizing the current collection of the thin-film-processed cathode was accomplished using an anode-supported SOFC with a thick-film (≈ 6 μm) YSZ electrolyte and a thin-film cathode. A substantial reduction in the contact loss was achieved during this study. It could now be asserted that the foundation has been laid to more accurately assess the anode-supported TF-SOFC properties.

On this basis, the ultimate performance level that a 1 μm-thick YSZ electrolyte-base NiO−YSZ anode-supported TF-SOFC can currently reach is reported in this study. A 1 μm-thick YSZ/200 nm-thick GDC bi-layer was chosen as the electrolyte due to the abundance of reference data available for comparison [16,22]. Lanthanum strontium cobaltite (LSC) was selected as the low-temperature high-performance oxide cathode material [24−26]. Two types of thin-film processed LSC-base cathodes were used. One is a single-phase LSC cathode fabricated via low-density film deposition and post-annealing. This type of cathode has been studied in numerous studies to investigate the limitations and potential of thin-film processed cathodes [23,27−29]. The other is a gradient-structured thin-film (GSTF) cathode based on an LSC−GDC nano-composite, which has been proved to be more structurally stable than the single phase LSC cathode [30]. The overall cell performance comparison and more detailed impedance analyses are presented to elucidate the difference between the electrode reactions.

2. Experimental

TF-SOFCs based on a 1 μm-thick YSZ electrolyte and a 200 nm-thick GDC buffer layer (bi-layer electrolyte) were fabricated on a compression-molded NiO−YSZ anode support with a screen-printed anode functional layer (C-SP anode). These C-SP anode supports were sintered at 1400 °C for 3 h. An NiO−YSZ nano-composite interlayer was deposited over the C-SP support using pulsed laser deposition (PLD) at a substrate temperature (T_s) of 700 °C and an ambient pressure (P_{amb}) for oxygen of 6.67 Pa. Afterward, the whole support structure was annealed at 1200 °C for 1 h to prevent Ni agglomeration during the reduction at the interlayer [31]. By controlling the surface quality of the C-SP support, 2−3 μm-thick interlayers could secure the gas-impermeability of the thin-film electrolyte. Both 1 μm-thick YSZ and 200 nm-thick GDC thin films were deposited over these interlayers at $T_s = 700$ °C and $P_{amb} = 6.67$ Pa. The process conditions for the YSZ-based TF-SOFC on the C-SP support are consistent with those from a previous work [16].

To fabricate a TF-SOFC with a single-phase LSC cathode, an LSC cathode layer was deposited on the GDC layer at room temperature using a $La_{0.6}Sr_{0.4}CoO_{3-\delta}$ (LSC64) target at $P_{amb} = 13.3$ Pa. The entire cell was post-annealed at 650 °C for 1 h to crystallize the LSC and produce a porous structure. The resulting cathode thickness was ~4.2 μm. The TF-SOFC with the single-phase LSC cathode will hereafter be denoted as TF-SOFC-S. The other TF-SOFC, which has a GSTF cathode, was fabricated as follows. A GSTF cathode composed of three layers, (1) an LSC64–GDC nano-composite layer deposited at $T_s = 700$ °C, $P_{amb} = 26.7$ Pa; (2) an LSC64–GDC nano-composite layer deposited at $T_s = 700$ °C, $P_{amb} = 40$ Pa; and (3) an LSC single layer deposited at room temperature, $P_{amb} = 13.3$ Pa, was formed over the GDC layer. The LSC64–GDC nano-composite layers were deposited using an LSC64–GDC composite target prepared by sintering a compacted mixed LSC64 and GDC powder pellet (mixing volume ratio = 1:1) at 1300 °C for 5 h. After the multilayer cathode deposition, the entire cell was post-annealed at 650 °C for 1 h to crystallize the top LSC layer. The resulting GSTF cathode thickness was ~4.4 μm, including ~3 μm-thick LSC–GDC nano-composite layer. The TF-SOFC with a GSTF cathode will hereafter be denoted as TF-SOFC-G. The fabrication process for the single-phase LSC and the GSTF cathodes are also described in previous work [30]. The microstructure of each cell was observed via scanning electron microscopy (SEM, XL-30 and Insfect F50, FEI).

During the fuel cell operation, air and humidified H_2 (3% H_2O) were used as the oxidant and fuel, respectively, and the flow rates of each were held constant at 200 sccm. A modified interconnect rib design with gold meshes with openings of 250 μm by 250 μm were used for the cell test. A cell test configuration with reduced contact loss is described in detail in a previous work [23]. The cell operating temperature varied from 650 to 500 °C at intervals of 50 °C, and the electrochemical impedance spectra (EIS) and current–voltage–power (I–V–P) curves were obtained at each temperature. A Solartron impedance analyzer with an electrochemical interface (SI1260 and SI1287, Solartron) and an Iviumstat electrochemical analyzer (Iviumstat, Ivium Technologies) were used to obtain these EIS and I–V–P curves, and each EIS was observed over a frequency range from 10^6 Hz to 10^{-1} Hz. The AC amplitude of the impedance measurements was 50 mV.

To investigate the difference between the electrode reaction mechanisms for two different cathodes in more detail, the EIS at several cell voltages with open circuit voltages (OCVs) of 0.75 V and 0.55 V were measured using various air to nitrogen flow ratios (200:0, 140:60, and 100:100 sccm; *i.e.*, 100, 70, and 50% air) at 600 °C. The hydrogen to nitrogen ratios were also varied on the anode side; however, the changes in the EIS were minor in comparison with that at the cathode as a function of the air variation, indicating that there is less significant impeding reaction at the anode at 600 °C, as is consistent with a previous report [16]. Hence, the fuel side variation results are not reported in detail in the present study.

3. Results and discussion

A schematic of the TF-SOFC cell after the fabrication, a picture of the fabricated unit cell, a cross-sectional micrograph of the TF-
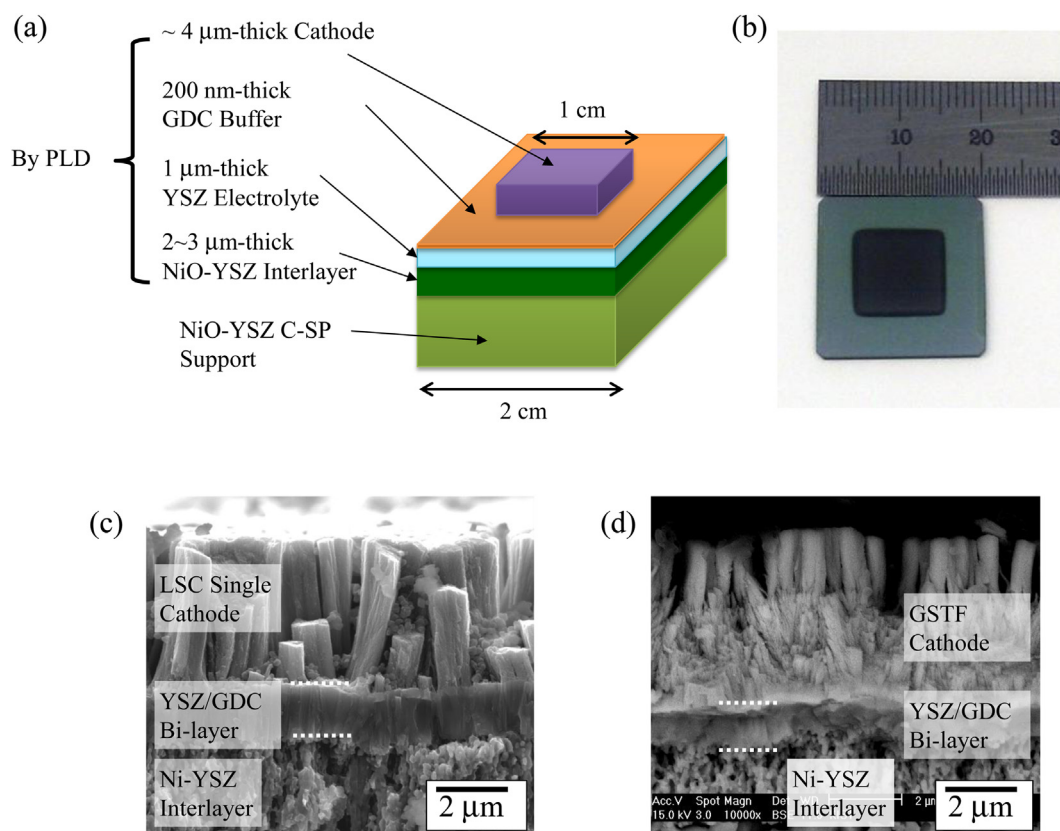

Fig. 1. (a) A schematic of the TF-SOFC on the anode support. (b) A picture of the TF-SOFC after fabrication. (c) Cross-sectional microstructure of the TF-SOFC-S. (d) Cross-sectional microstructure of the TF-SOFC-G.

Table 1
Ohmic ASR values for the bi-layer electrolytes, TF-SOFC-S, TF-SOFC-G, and TF-SOFC, from Ref. [16].

Temp. (°C)	Calculated ASR of 1 μm-thick YSZ/200 nm-thick GDC [mΩ cm²]	Ohmic ASR of TF-SOFC-S [mΩ cm²]	Ohmic ASR of TF-SOFC-G [mΩ cm²]	Ohmic ASR of TF-SOFC [16] [mΩ cm²]
650	12	37	37	
600	30	53	47	96
550	62	80	67	140
500	134	167	123	282

SOFC-S, and one of the TF-SOFC-G after the cell tests are shown in Fig. 1(a)–(d), respectively. As indicated in Fig. 1(a), all the cell components except for the support were fabricated using PLD, which implies that TF-SOFCs based on this platform can be sequentially processed using currently available thin-film techniques. The nanostructured NiO–YSZ anode interlayer, YSZ electrolyte and GDC buffer layers covered the entire surface of the 2 cm by 2 cm anode support, and the cathode area was 1 cm by 1 cm as shown in Fig. 1(b). This cell area is substantially larger than that of the TF-SOFCs on free-standing membranes [3,11] and is only limited by the uniform coverage area of the used PLD apparatus used in this study. The cell testing configuration for the optimum current collection consists of a metallic interconnect with a modified rib design and Ni-foams and gold meshes as contact materials [23], and a compression seal based on glass–ceramic composite [32] is used. No noble metal paste was used to facilitate the electrical contact or current collection; therefore, the testing configuration is nearly identical to that of a conventional anode-supported SOFC cells and stack [32,33] except for its size.

In Fig. 1(c) and (d), the cell structures of the TF-SOFC-S and TF-SOFC-G are shown. It was confirmed that both cells exhibited identical microstructural characteristics of the anode-supported TF-SOFC up to the electrolyte, i.e., a fully dense and hetero-epitaxial YSZ/GDC bi-layer electrolyte and a nanostructured interlayer with a grain size about 100 nm formed over the anode support with the micrometer-scale microstructure. Detailed features can be found in previous reports [16,17,34]. Since the microstructures were observed after the cell test, the NiO–YSZ interlayer was turned into nanoporous Ni–YSZ due to the reduction during the cell test. The microstructural differences of the single phase cathode and the GSTF cathode are shown clearly in Fig. 1(c) and (d).

The ASR values of the bi-layer electrolyte (calculated from the measured conductivity of each thin film), ohmic ASRs of both the TF-SOFC-S and TF-SOFC-G, and that of TF-SOFC from a previous report [16] are compared in Table 1. The previously reported TF-SOFC values [16] are for the same half cell up to the bi-layer electrolyte and a 1 μm-thick single phase LSC cathode, and the cell performance was measured using the original setup, which was not optimized to reduce contact losses. Considering that the ohmic ASR of the cells did not change much when the cathode thickness was varied from 1 to 3 μm [27], it can be assumed that the ohmic ASR reduction originates from the improved cell test configuration. A substantial decrease in the ohmic ASRs relative to the previous setup is obvious. Between the two cells, TF-SOFC-G exhibits slightly lower ohmic ASR values than TF-SOFC-S. As can be seen in Fig. 1(c) and (d), the cathode domains in the single-phase LSC cathode are widely separated, while the composite layer in the GSTF cathode is denser and more continuous. Thus, the lateral conduction loss of the single phase LSC cathode may be larger than that of the GSTF cathode. Nonetheless, the substantially reduced ohmic ASR values
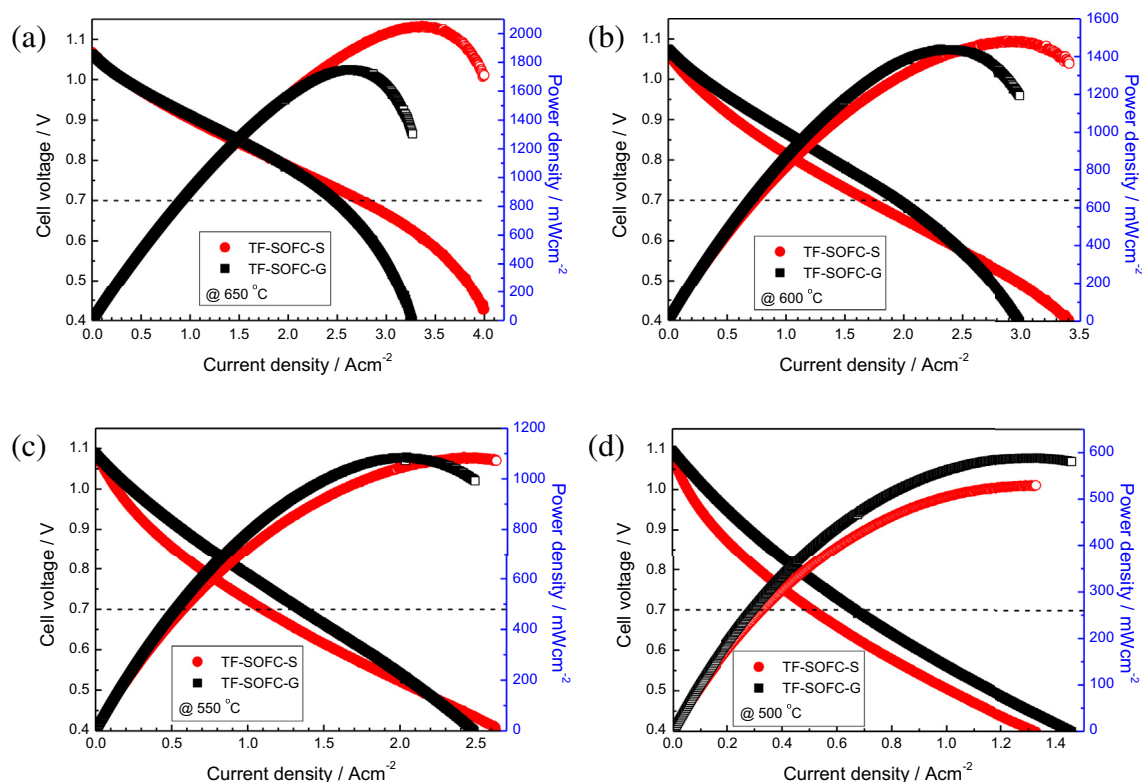

Fig. 2. I–V–P curves of the TF-SOFC-S (red circle) and TF-SOFC-G (black square) at each temperature: (a) 650 °C, (b) 600 °C, (c) 550 °C, and (d) 500 °C. Horizontal dashed lines are at V = 0.7 V. (For interpretation of the references to color in this figure legend, the reader is referred to the web version of this article.)

Table 2
Power density values for the TF-SOFC-S and TF-SOFC-G at each operating temperature.

Temp. (°C)	Power density at 0.7 V [mW cm^{-2}]		Peak power density [mW cm^{-2}]	
	TF-SOFC-S	TF-SOFC-G	TF-SOFC-S	TF-SOFC-G
650	1920	1733	2048	1746
600	1189	1369	1480	1437
550	772	943	1084	1087
500	358	466	529	588

measured for both of the cells in the modified setup allow for a more precise measurement of the TF-SOFCs.

The $I–V–P$ curves of each TF-SOFC at each temperature, measured at the improved test configuration, are shown in Fig. 2. The power density at 0.7 V and peak power density for both cells at each temperature are listed in Table 2. When performance losses originating from external factors are minimized, the low-temperature performance of the anode-supported TF-SOFC reaches a high level. The power density of the TF-SOFC-G at 0.7 V and 600 °C reaches 1369 mW cm^{-2}, which approaches the projected (extrapolated) value from a previous report [21] and is over a 1.8 times improvement relative to previously reported values based on the same platform [16]. The peak power densities of both cells reach over 500 mW cm^{-2} at 500 °C. To our knowledge, this is the highest low-temperature performance ever reported for a YSZ-based anode-supported SOFC. Even the obtained performance of the TF-SOFCs was better than that of a previously reported free-standing-membrane-base TF-SOFC with the same electrolyte materials (YSZ) and dimensions ($\sim$1 µm) by authors [11] (350 mW cm^{-2} at 500 °C). Considering that an infinitesimally thin gas-impermeable electrolyte layer cannot form over the porous anode support, it is believed that the performance presented in this work is at a substantially high level that the YSZ-based SOFC can reach when using the common SOFC materials (YSZ, GDC, LSC, NiO–YSZ) and platforms (NiO–YSZ anode supports) and only changing the dimension of the cell components.

Comparing the $I–V–P$ curves of the TF-SOFC-S and TF-SOFC-G reveal certain interesting trends. At 650 °C, the $I–V$ curves look nearly identical for low current densities (less than 2 A cm^{-2}); however, the voltage drop becomes considerably more rapidly for the TF-SOFC-G above a certain current (Fig. 2(a)). As a result, the power density at 0.7 V and peak power density is much lower for the TF-SOFC-G at 650 °C than for the TF-SOFC-S. As the temperature decreases, these trends start to change. At 600 °C and 550 °C (Fig. 2(b) and (c), respectively), the decrease in the $I–V$ curve for TF-SOFC-G is smaller than for TF-SOFC-S at the low current density range; however, it becomes larger in high current density regime. Therefore, the power density at 0.7 V of TF-SOFC-G surpasses that of TF-SOFC-S at these temperatures, but the peak power density of the TF-SOFC-G remains lower than or similar to that of TF-SOFC-S. At 500 °C, both the power density at 0.7 V and peak power density of TF-SOFC-G are higher than those of TF-SOFC-S. Because the two cells are identical up to the GDC buffer layer, these differences must originate from the cathode reaction. It is therefore worthwhile to investigate the cathode reaction of these cells in more detail.
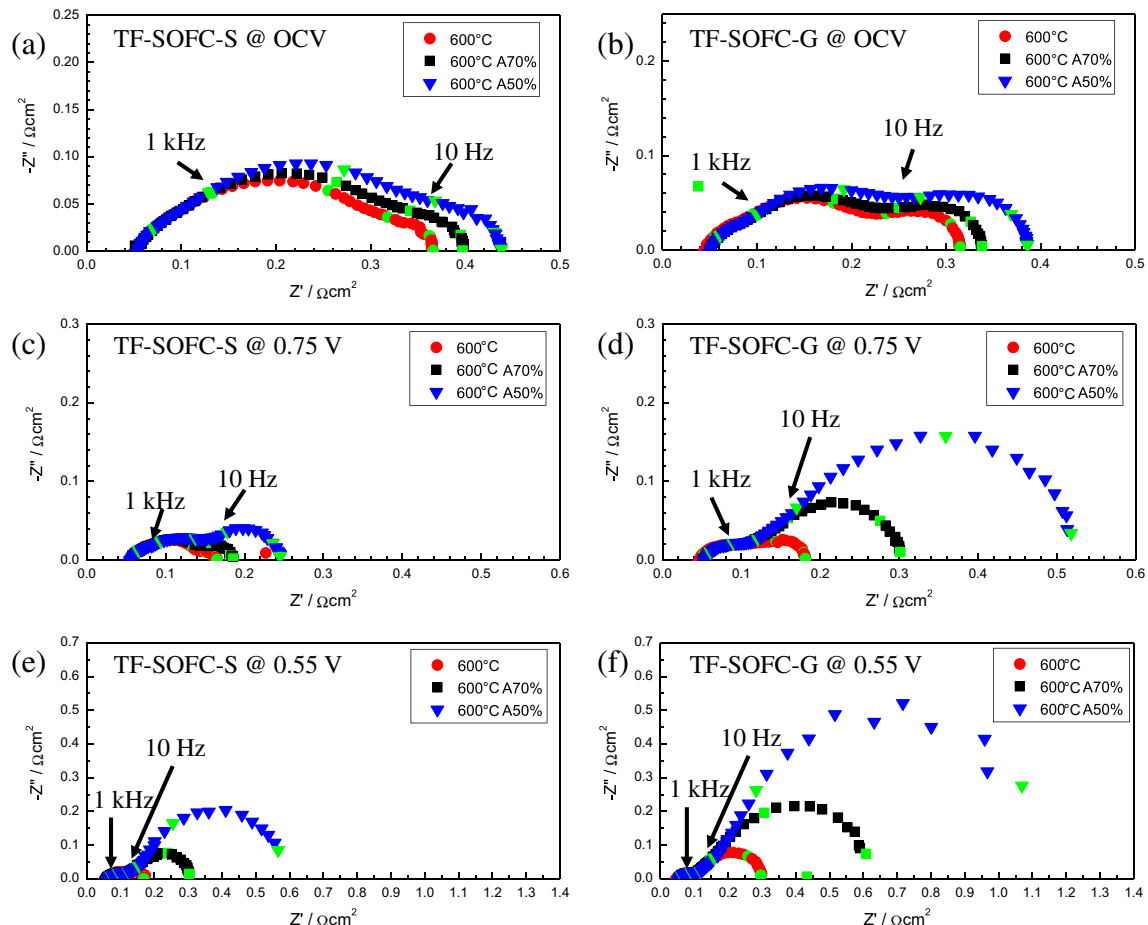

Fig. 3. Nyquist plots of the TF-SOFC-S (left) and TF-SOFC-G (right) for varying air supply ratios measured at cell voltages of a), b) OCV; c), d) 0.75 V; and e), f) 0.55 V, at 600 °C.

Because 600 °C is the temperature at which the transition of the above-mentioned trends becomes the most obvious, the impedance analyses at 600 °C were performed the most rigorously in this present work. Fig. 3 compares the Nyquist plots of the EIS for TF-SOFC-S and TF-SOFC-G at OCV of 0.75 V and 0.55 V side by side. Each EIS graph contains three curves measured when 100%, 70%, and 50% air (nitrogen balance, at 200 sccm) is supplied to the cathode side. As mentioned in Experimental section, the hydrogen to nitrogen ratios at the anode side were also varied, and the EIS of both cells only changed slightly in the frequency range from $f \leq 10$ Hz at 600 °C, indicating there was little limitation to the gas transport and no other significant impeding reaction at the anode, similar to what was reported in a previous study [16].

As the air supply changes, the impedance in the frequency range for $f \leq 1$ kHz is affected. The low-frequency (LF) range of $f \leq 10$ Hz reportedly corresponds to gas transport, and the mid-frequency (MF) range of 10 Hz $\leq f \leq 1$ kHz is allocated to oxygen surface exchange and oxygen ion diffusion at the cathode [16,29]. Comparing the EIS at the OCV, the MF arc size of the TF-SOFC-G is smaller than that of the TF-SOFC-S; however, the LF arc size is bigger. These results imply that the cathodic activity of the GSTF cathode may be superior to that of the room temperature-deposited and post-annealed single-phase LSC, while the gas transport of the former is more severely impeded. As the cell voltage decreases (i.e., current density increases), the gas transport becomes a more impeding process because more gas species are consumed by the fuel cell reaction. Therefore, if the gas transport is a significant impeding factor, reducing the air supply would create more readily apparent changes at lower cell voltages (higher current density). Fig. 3(c)–(f) shows that the LF arcs become larger and are more greatly affected by the air reduction in both cells.

However, as predicted, the LF arc of the TF-SOFC-G become much larger and is more seriously affected by the changes to air (Fig. 3(d) and (f)). These results augment the aforementioned assumptions.

The electrode reactions of two cells can be more clearly discerned using Bode plots. In Fig. 4, Bode plots of the EIS for two cells with OCVs of 0.75 V and 0.55 V are compared (air supply 100%) at 600 °C. In the MF range, especially at $f \geq 100$ Hz, the impedance of the TF-SOFC-G is lower for all cell voltages. Therefore, at the OCV, the impedance of the TF-SOFC-G is smaller for all frequency ranges. For LF, the impedance increment of the TF-SOFC-G as the cell voltage lowers is higher than for the TF-SOFC-S. Again, the Bode plots indicate that the cathodic properties related to the oxygen exchange and oxygen ion diffusion of the GSTF cathode are superior to those of single-phase LSC cathode. This is why the drop in the I–V curve in lower current density regime is less than for TF-SOFC-G, i.e., the activation loss of the GSTF cathode is less than that of the single-phase LSC cathode. In contrast, the gas transport is significantly impeded at the GSTF cathode. As can be seen in Fig. 1(d), the GSTF cathode has a much denser composite layer and, although the thickness is low, it appears that the density of the composite layers still impede the gas transport at high current density. According to previous reports on the GSTF cathode [30], high-temperature deposition provides a much stronger interface and, as a result, betters long-term stability. At the same time, however, a high-temperature deposition increases the density of the layer and impedes gas transport. To fully use the GSTF cathode therefore requires a more careful structural design and control of the process conditions.

Although the cathode activity could be improved by using the GSTF cathode, further improvements to the electrode properties are required to further enhancement the current low-temperature
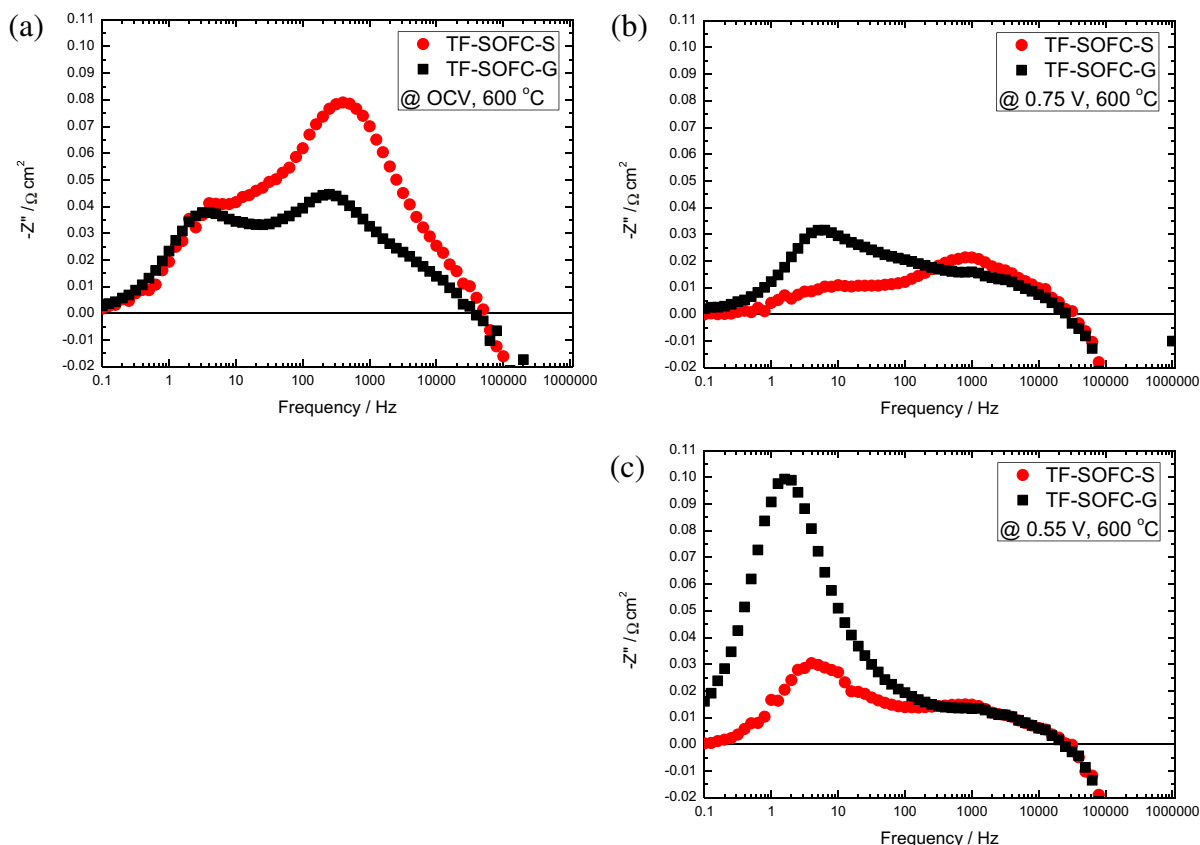

Fig. 4. Bode plots of TF-SOFC-S (circle) and TF-SOFC-G (square) with cell voltages of (a) OCV, (b) 0.75 V, and (d) 0.55 V, at 600 °C.

Table 3
Pol. ASR values and the ratio of the Pol. ASR to the ohmic ASR for TF-SOFC-S and TF-SOFC-G at each operating temperature.

Temp. ($^{\circ}$C)	Pol. ASR of TF-SOFC-S [mΩ cm^2]	Pol. ASR to ohmic ASR ratio of TF-SOFC-S	Pol. ASR of TF-SOFC-G [mΩ cm^2]	Pol. ASR to ohmic ASR ratio of TF-SOFC-G
650	217	5.86	192	5.19
600	310	5.89	268	5.70
550	641	8.01	358	5.34
500	1585	9.49	704	5.72

performance. Table 3 lists both the pol. ASR values of the TF-SOFC-S and TF-SOFC-G the OCV and the ratio of the pol. ASR to the ohmic ASR at each temperature. Improving the cathodic activity decreases the exhibited TF-SOFC-G pol. ASR more than the TF-SOFC-S at the OCV. Still, the pol. ASR is more than 5 times larger than the ohmic ASR at all temperatures. These findings mean that the electrolyte resistance only provides approximately 15% of the total ASR at best when the thin film electrolyte is successfully implemented. Even if the electrolyte thickness is further reduced and/or alternative highly conductive electrolyte materials are employed, the impact on the cell performance would be limited unless an improvement to the electrode was also provided.

4. Conclusions

Minimizing the performance losses caused by external factors makes a more precise assessment of the low-temperature performance of the YSZ-based anode-supported TF-SOFC possible. The peak power density of the YSZ-electrolyte-base TF-SOFC at 500 $^{\circ}$C reaches over 500 mW cm^{-2}, which is unprecedented for YSZ-based anode-supported SOFCs. A more detailed analysis of the electrode reactions in the thin-film processed cathodes is also enabled, and the cathodic reaction between the single-phase LSC and GSTF cathode are systematically compared and correlated to the cell performance.

The EIS analyses yield the following results both in terms of the thin-film electrolyte and the nanostructured electrodes for the low-temperature operation of SOFCs:

1. The electrolyte contribution to the total cell performance loss is limited, provided that the thin-film electrolyte is successfully constructed. It is more important to the critical low-temperature performance of the SOFC to improve the electrodes, especially the cathode.
2. In this study, nano-structure LSC-base cathodes, one of the most active SOFC cathode materials currently available is used. Further improvements in the low-temperature performance of the cathode, should therefore be considered. Developing innovative cathode materials and/or the usage of the metallic catalysts may be a possible solution. When using metallic catalysts, the structural instability of the metallic catalysts at elevated temperature should be resolved for reliable operations.

References

[1] E.D. Wachsman, K.T. Lee, Science 334 (2011) 935–939.
[2] A. Bieberle-Hutter, D. Beckel, A. Infortuna, U.P. Muecke, J.L.M. Rupp, L.J. Gauckler, S. Rey-Mermet, P. Muralt, N.R. Bieri, N. Hotz, M.J. Stutz, D. Poulikakos, P. Heeb, P. Muller, A. Bernard, R. Gmur, T. Hocker, J. Power Sources 177 (2008) 123–130.
[3] C.-C. Chao, C.-M. Hsu, Y. Cui, F.B. Prinz, ACS Nano 5 (2011) 5692–5696.
[4] H. Huang, M. Nakamura, P.C. Su, R. Fasching, Y. Saito, F.B. Prinz, J. Electrochem. Soc. 154 (2007) B20–B24.
[5] K. Kerman, B.-K. Lai, S. Ramanathan, J. Power Sources 196 (2011) 2608–2614.
[6] P.C. Su, C.C. Chao, J.H. Shim, R. Fasching, F.B. Prinz, Nano Lett. 8 (2008) 2289–2292.
[7] J.H. Shim, C.C. Chao, H. Huang, F.B. Prinz, Chem. Mater. 19 (2007) 3850–3854.
[8] M. Tsuchiya, B.-K. Lai, S. Ramanathan, Nat. Nanotechnol. 6 (2011) 282–286.
[9] U.P. Muecke, D. Beckel, A. Bernard, A. Bieberle-Hutter, S. Graf, A. Infortuna, P. Muller, J.L.M. Rupp, J. Schneider, L.J. Gauckler, Adv. Funct. Mater. 18 (2008) 3158–3168.
[10] A. Evans, A. Bieberle-Hütter, J.L.M. Rupp, L.J. Gauckler, J. Power Sources 194 (2009) 119–129.
[11] C.-W. Kwon, J.-W. Son, J.-H. Lee, H.-M. Kim, H.-W. Lee, K.-B. Kim, Adv. Funct. Mater. 21 (2011) 1154–1159.
[12] C.-W. Kwon, J.-I. Lee, K.-B. Kim, H.-W. Lee, J.-H. Lee, J.-W. Son, J. Power Sources 210 (2012) 178–183.
[13] A. Evans, M. Prestat, R. Tölke, M.V.F. Schlupp, L.J. Gauckler, Y. Safa, T. Hocker, J. Courbat, D. Briand, N.F. de Rooij, D. Courty, Fuel Cells 12 (2012) 614–623.
[14] C.D. Baertsch, K.F. Jensen, J.L. Hertz, H.L. Tuller, S.T. Vengallatore, S.M. Spearing, M.A. Schmidt, J. Mater. Res. 19 (2004) 2604–2615.
[15] X.H. Wang, H. Huang, T. Holme, X. Tian, F.B. Prinz, J. Power Sources 175 (2008) 75–81.
[16] H.-S. Noh, H. Lee, B.-K. Kim, H.-W. Lee, J.-H. Lee, J.-W. Son, J. Power Sources 196 (2011) 7169–7174.
[17] D.-H. Myung, J. Hong, K. Yoon, B.-K. Kim, H.-W. Lee, J.-H. Lee, J.-W. Son, J. Power Sources 206 (2012) 91–96.
[18] E.-O. Oh, C.-M. Whang, Y.-R. Lee, S.-Y. Park, D.H. Prasad, K.J. Yoon, J.-W. Son, J.-H. Lee, H.-W. Lee, Adv. Mater. 24 (2012) 3373–3377.
[19] T. Suzuki, Z. Hasan, Y. Funahashi, T. Yamaguchi, Y. Fujishiro, M. Awano, Science 325 (2009) 852–855.
[20] T. Suzuki, M.H. Zahir, T. Yamaguchi, Y. Fujishiro, M. Awano, N. Sammes, J. Power Sources 195 (2010) 7825–7828.
[21] F. Han, R. Mücke, T. Van Gestel, A. Leonide, N.H. Menzler, H.P. Buchkremer, D. Stöver, J. Power Sources 218 (2012) 157–162.
[22] H.-S. Noh, J.-W. Son, H. Lee, H.-S. Song, H.-W. Lee, J.-H. Lee, J. Electrochem. Soc. 156 (2009) B1484–B1490.
[23] H.-S. Noh, J. Hwang, K. Yoon, B.-K. Kim, H.-W. Lee, J.-H. Lee, J.-W. Son, J. Power Sources 230 (2013) 109–114.
[24] H.-I. Ji, J. Hwang, K.J. Yoon, J.-W. Son, B.-K. Kim, H.-W. Lee, J.-H. Lee, Energy Environ. Sci. 6 (2013) 116–120.
[25] H.-G. Jung, Y.-K. Sun, H.-Y. Jung, J.-S. Park, H.-R. Kim, G.-H. Kim, H.-W. Lee, J.-H. Lee, Solid State Ionics 179 (2008) 1535–1539.
[26] M. Kubicek, Z. Cai, W. Ma, B. Yildiz, H. Hutter, J. Fleig, ACS Nano 7 (2013) 3276–3286.
[27] H.-S. Noh, H. Lee, H.-I. Ji, H.-W. Lee, J.-H. Lee, J.-W. Son, J. Electrochem. Soc. 158 (2011) B1–B4.
[28] H.-S. Noh, J.-W. Son, H. Lee, J.-S. Park, H.-W. Lee, J.-H. Lee, Fuel Cells 10 (2010) 1057–1065.
[29] J. Hwang, H. Lee, K.J. Yoon, H.-W. Lee, B.-K. Kim, J.-H. Lee, J.-W. Son, J. Electrochem. Soc. 159 (2012) F639–F643.
[30] D.-H. Myung, J. Hwang, J. Hong, H.-W. Lee, B.-K. Kim, J.-H. Lee, J.-W. Son, J. Electrochem. Soc. 158 (2011) B1000–B1006.
[31] H.-S. Noh, J.-W. Son, H. Lee, H.-I. Ji, J.-H. Lee, H.-W. Lee, J. Eur. Ceram. Soc. 30 (2010) 3415–3423.
[32] J.-H. Lee, H. Kim, S.M. Kim, T.-W. Noh, H.-Y. Jung, H.-Y. Lim, H.-G. Jung, J.-W. Son, H.-R. Kim, B.-K. Kim, H.-J. Je, J.-C. Lee, H. Song, H.-W. Lee, Adv. Energy Mater. 2 (2012) 461–468.
[33] H.-Y. Jung, S.-H. Choi, H. Kim, J.-W. Son, J. Kim, H.-W. Lee, J.-H. Lee, J. Power Sources 159 (2006) 478–483.
[34] H.-S. Noh, J.-S. Park, H. Lee, H.-W. Lee, J.-H. Lee, J.-W. Son, Electrochem. Solid State Lett. 14 (2011) B26–B29.